Chapter 5

Toughening of Low-Alloy Steel by Ultrafine-Grained Structure (Development of Fracture Control from Microstructure Design)

Tadanobu Inoue

Additional information is available at the end of the chapter

http://dx.doi.org/10.5772/63797

Abstract

Microstructural design for improving the strength–toughness balance was studied in low-alloy steel. Medium-carbon steel bars with microstructures of two types such as an ultrafine elongated grain (UFEG) structure and an ultrafine equiaxed grain (UFG) structure were fabricated by multi-pass warm caliber rolling and subsequent annealing. Conventionally, quenched and tempered steel with a martensitic structure and low-carbon steel with a ferrite–pearlite structure were also prepared. The tensile and three-point bending tests were conducted for all samples. In particular, the fracture behavior after the bending test was observed in detail and investigated, including the effect of microstructure features. As a result, the strength–toughness balance of the UFEG steel was excellent compared with that of all other steels. The present results provide useful guidelines for designing microstructure to improve the strength–toughness balance in metallic materials.

Keywords: iron and steel, strength–toughness balance, grain refinement, anisotropic properties, crack propagation

1. Introduction

Strong and tough materials are always needed in order to improve safety and performance and to reduce weight in transportation and heavy machinery. It is not difficult to achieve high strength with the help of the current materials science and technology. However, as shown in **Figure 1**, strength and toughness in materials have a strong relation, and toughness decreases with increasing strength, that is, strengthening of materials deteriorate toughness [1]. Few

structural metallic materials are limited by their strength; rather, they are limited by their fracture toughness. Unfortunately, most of materials research is still focused on the quest for high strength.

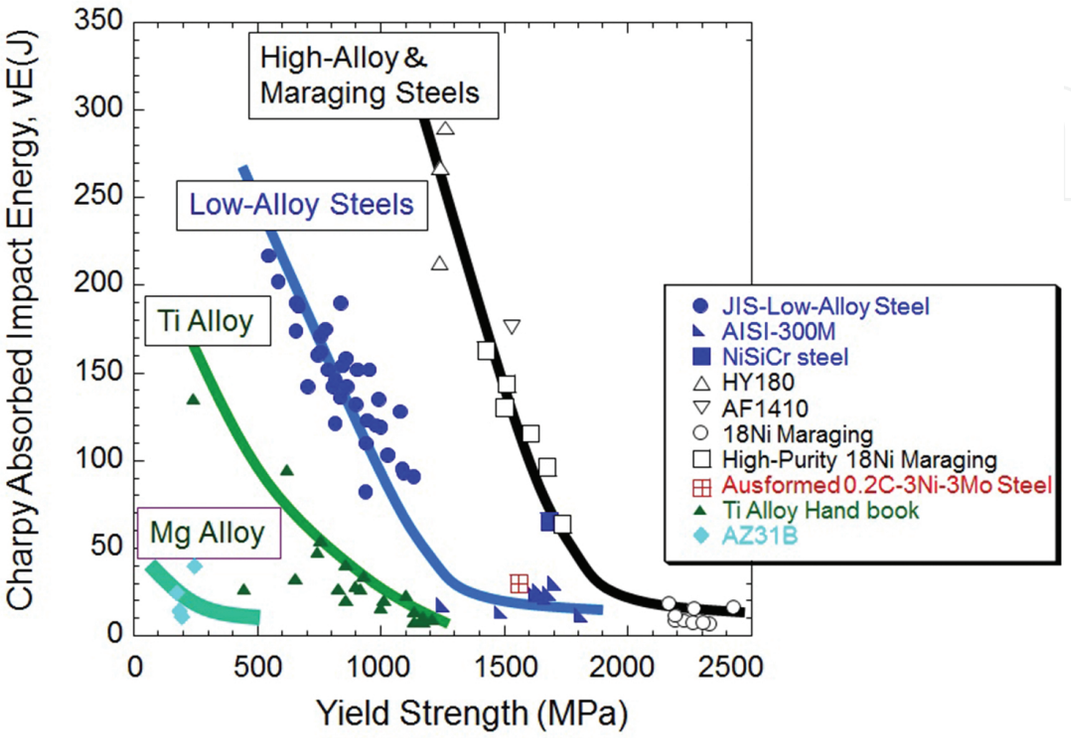

Figure 1. Correlation between yield strength and Charpy full-size V-notch impact energy at ambient temperature in structural metallic materials.

It was believed that refinement of crystal grains is an effective method for developing strength and toughness in metallic materials without the addition of alloying elements; hence, ultrafine-grained (UFG) materials are very attractive in materials science [2–4]. However, although a refinement of crystal grain until submicronsized or nanosized grains are obtained normally leads to higher strength on the basis of the Hall–Petch relation [4, 5], it does not always lead to the improvement of toughness. Many results [5–9] indicated that the ductile-to-brittle transition (DBT) temperature of bcc steels accompanied by a change in the fracture mechanism from void coalescence to cleavage was improved by grain refinement, although the upper-shelf energy became lower due to a decrease in ductility by strength enhancement. However, for such UFG steels produced through severe plastic deformation processes, the relaxation of the triaxial tension toward a state of biaxial tension resulting from the presence of separations of the crack-divider type (see **Figure 2a**) appears to be one of the reasons [10, 11]. The fracture of this type has often been observed elsewhere, such as in rolled steel pipes and plates and Al–Li alloys, and it leads to the improvement of toughness at low temperatures because of relaxation of the triaxial tension stresses generated by the localized plastic constraint at the crack tip. Bourell [12] showed that for low-carbon steel, the separations markedly appeared with increasing strain and decreasing temperature due to the development of {1 0 0}<1 1 0>

http://dx.doi.org/10.5772/63797

texture in a rolled sheet. As a result, the upper shelf energy in the sheet decreased and the lower shelf energy increased. The microstructure in Al–Li alloys used for the main fuel tank of the space shuttle was pancake-shaped grains elongated in the rolling direction, and the alloys had high toughness at liquid helium temperatures [13, 14]. This is due to delamination toughening of crack-divider type, which is caused by the weak sites, such as the segregation to grain boundaries and coarse Fe–Cu- or Mg–Cu-rich constituent particles.

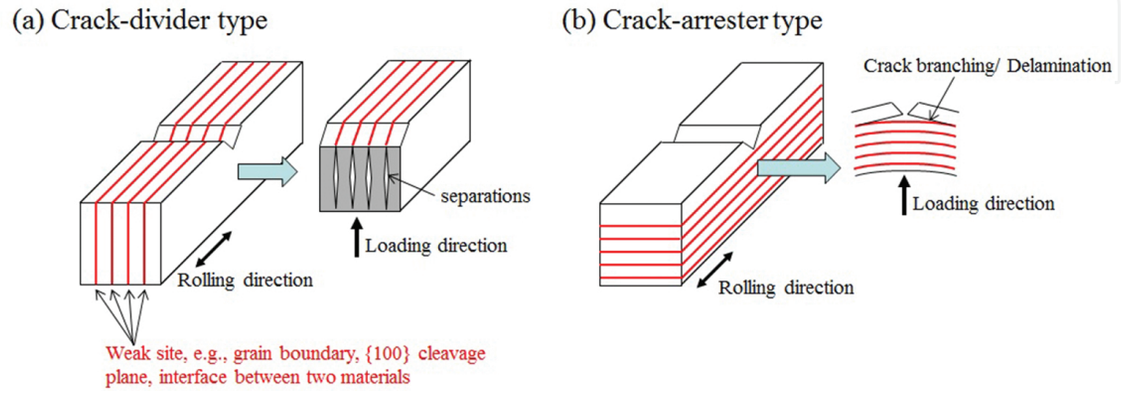

Figure 2. Fracture types of delamination/splitting in anisotropic material containing specific planes of weakness in one direction.

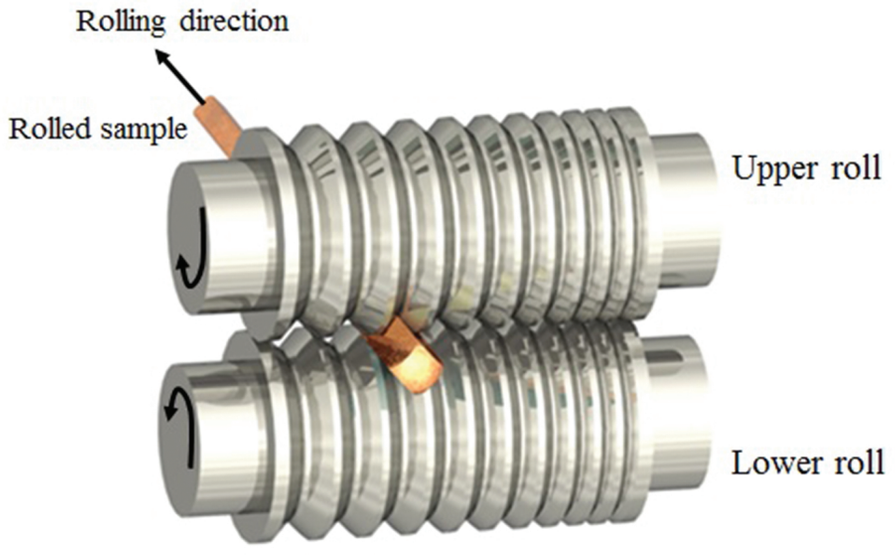

Figure 3. Schematic drawing of the caliber rolling with square grooves.

In our studies, warm caliber rolling (WCR) shown in **Figure 3** has been proposed as a deformation process to fabricate bulk UFG bars with a length of over 1000 mm, and this process has already been reported to be effective for producing various metallic materials with UFG structures. In these studies, a medium-carbon low-alloy steel of 1800 MPa tensile strength level with ultrafine elongated grain (UFEG) structures showed an inverse temperature dependence

of toughness in the Charpy V-notch impact tests [2]. In addition, in a low-carbon low-alloy steel of 800 MPa strength with UFEG structures, the strength increased with the decrease in thickness of the elongated ferrite grain structures, and the upper-shelf energy was maintained until a low temperature was reached [15]. These toughening are attributed to mechanisms of the crack arrester type (see **Figure 2b**), which arrests the propagation of main cracks. However, in case of impact toughness such as the Charpy test, it is difficult to clarify the fracture behavior because the occurrence, propagation, and linkage of microcracks are caused almost simultaneously during the impact loads. And, the property of toughness is sensitive to not only the size of crystal grains but also their orientation and shape. It is of interest to systematically study the strength–toughness balance on the static fracture toughness in UFG steel, the effect of microstructure features with respect to its balance and fracture behaviors including crack propagation.

In this chapter, medium-carbon steel bar with UFEG structure is fabricated by multi-pass WCR, and steel bar with UFG structure is created by subsequent annealing. Also, two conventional steels, medium-carbon steel with a martensitic structure and low-carbon steel with a ferrite–pearlite structure are prepared. First, a three-point bending test is conducted at ambient temperature, the fracture behaviors of each sample are compared, including bending load–displacement curves and microstructure observation of crack propagation from the initial notch. Next, the three-point bending test is conducted at a temperature range from 200 to −196°C, and the effect of the heterogeneous microstructure is examined based on the strength–toughness balance as well as fracture behavior.

2. Experimental procedure

2.1. Specimen preparation

A chemical composition of medium-carbon steel used in this study is Fe–0.39C–2.01Si–1.02Cr–1.0Mo–0.21Mn–0.004Al–0.0022N–0.001O–<0.001P–<0.001S (all in mass pct). A 100-kg ingot was prepared by vacuum melting and casting, homogenized at 1200°C, and then hot rolled to a 40-mm-thick plate. A block of 40 × 120 L mm^3 was cut out of the plate, solution-treated at 1200°C for 3600 s and then hot rolled into a bar of about 31 mm^2, followed by water quenching. The quenched bar was soaked at 500°C for 1 h, subjected to a caliber rolling simulator [16] without any lubricant, and then air cooled. Eventually, a 14.3 × 930 L mm^3 rolled bar was fabricated. Hereafter, this sample is designated as *the TF sample*. To clarify the shape effect of crystal grains on the strength–toughness balance, the TF sample was annealed at 700°C for 1 h [2]. Hereafter, this sample is designated as *the TFA sample*. For comparison, conventional steels of *the QT sample* and *the SM490 sample* were prepared. To fabricate the QT sample with a martensitic structure, a bar was solution-treated at 950°C for 0.5 h, followed by oil quenching, tempered at 500°C for 1 h and then water cooled. The SM490 sample with a ferrite–pearlite structure in a chemical composition of 0.15C–0.3Si–1.5Mn was heated to 900°C and held for 1 h, followed by air cooling [15]. The principal axes of the rolled bar in this study are defined as shown in **Figure 4a**.

http://dx.doi.org/10.5772/63797

2.2. Microstructure and mechanical properties

The appearance of specimens after the three-point bending test was observed through a digital camera, and fracture surfaces were observed through a scanning electron microscope (SEM) operated at 15 kV. The microstructures at the central parts in the rolled bars were observed using the electron backscattered diffraction (EBSD) method in an SEM equipped with a field emission gun.

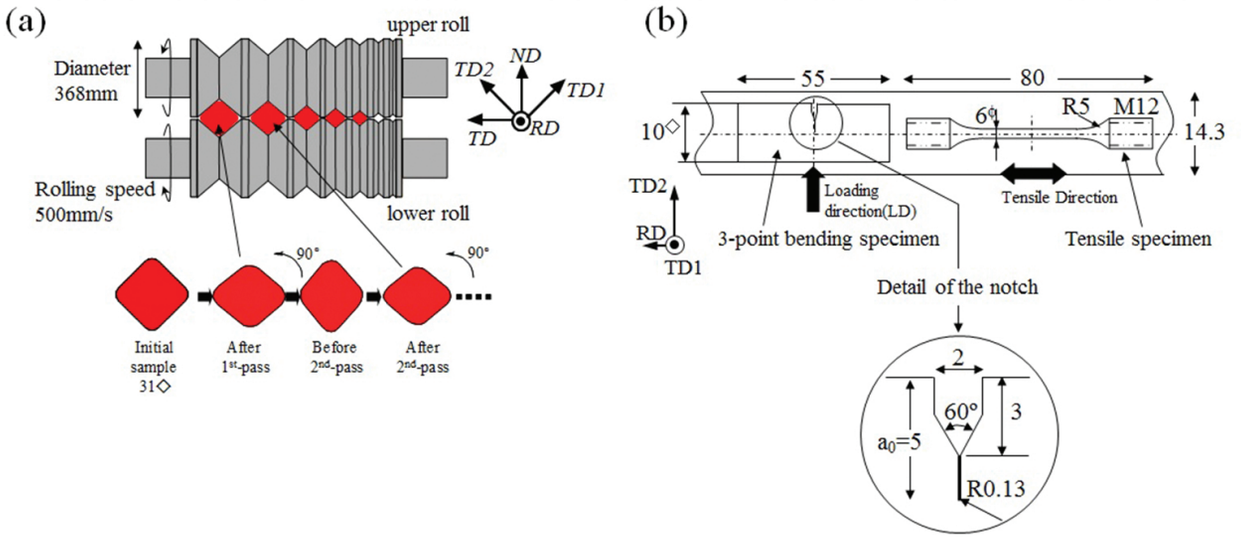

Figure 4. (a) Schematic drawing of the caliber rolling used in the present study and (b) position relation between a rolled bar in a 14.3 mm^2, a three-point bending specimen in a 10 mm^2, and tensile specimen in round type.

All mechanical test samples were taken from the center in the rolled bars, as shown in **Figure 4b**. Tensile tests were conducted with a crosshead speed of 0.85 mm/min (initial strain rate 5 × 10^{-4}/s) using specimens with a round cross section of 6 mm and a gage length of 30 mm. To prepare single-edge bend specimens in a three-point bending test, rectangular bars of 10W × 10B ×55L mm^3 were first machined along the RD, and then a notch with a depth of a_0 = 5 mm and a root radius of 0.13 μm as illustrated in **Figure 4b** was introduced using electro-discharge machining with fine wire 0.2 mm in diameter. A three-point bending test with a support distance of 40 mm at a crosshead speed of 0.5 mm/min was conducted at a temperature range of 23 and −196°C in the QT, TFA, and SM490 samples and a range of 200 and −196°C in the TF sample. The test was terminated when the specimen fractured completely or the displacement reached 10 mm, which corresponds to the specimen thickness. Nonlinear fracture mechanics methods on the basis of ASTM Standard E1820-01 were used to evaluate the fracture toughness. The apparent fracture energy, J (KJ/m^2), was calculated through the following formula:

$$J = 2\frac{A_{pl}}{Bb} = \frac{2}{Bb}\int_0^{u_a} P\,du$$

where A_{pl} is the area under the *P*-*u* curve, *B* is the specimen thickness, *b* is the ligament length (W-a_0), and u_a denotes the displacement at which the test was terminated. All the values presented are an average of two to four measurements.

3. Results

3.1. Microstructure evolution

The orientation maps for the QT, TF, and TFA samples and an SEM image for the SM490 sample are shown in **Figure 5**. The QT sample has a martensitic structure of a random crystallographic orientation, as shown in **Figure 5a**. On the other hand, the TF and TFA samples have a strong α-fiber texture parallel to the RD, that is, RD//<1 1 0>, as shown in **Figure 5b** and **c**. There are no significant differences in texture between the TF and TFA samples despite the annealing treatment. In the TF sample, the average of transverse linear interceptions for the elongated grains with misorientation angles of more than 10° was 310 nm. Furthermore, spheroidal nanosized carbide particles of 50 nm and below were dispersed in the elongated grain matrix [17]. In the TFA sample which resulted in the development of a granular grain structure, the transverse size of the ferrite grains increased to 660 nm. Relatively large carbide particles (200–300 nm) appeared to exist on the grain boundaries, while finer carbide particles were dispersed in the grain matrix. On the other hand, the distributions of Kernel average misorientation, KAM, which has a strong correlation with the dislocation densities within the cell interior of the deformed structures, were analyzed from electron backscatter patterns (EBSP) maps shown in **Figure 5b** and **c**. The average value of KAM for the TF and TFA samples was 0.65° and 0.38°,

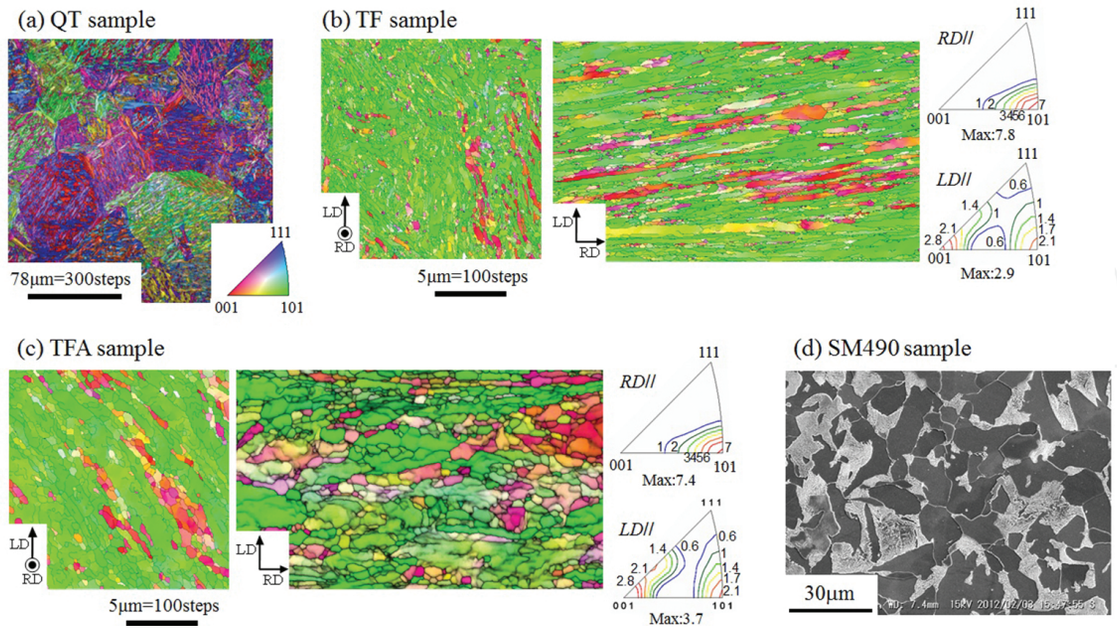

Figure 5. Orientation maps on cross-sectional plane for (a) QT, (b) TF, and (c) TFA samples by EBSD analysis and (d) an SEM image of SM490 sample.

http://dx.doi.org/10.5772/63797

respectively. This indicated that the dislocation density for the TF sample was somewhat larger than that for the TFA one. In the SM490 sample, the average size of the ferrite grain in **Figure 5d** was approximately 20 μm [18].

3.2. Mechanical properties

3.2.1. Mechanical properties at ambient temperature

The static mechanical properties, including fracture toughness, *J*, at ambient temperature, are summarized in **Table 1**. The TF sample with UFEG structure exhibited superior ductility, despite the high yield strength. Generally, the plastic instability or necking during tensile tests occurred immediately after the tensile stress reached the yield point by grain refinement. However, the TF and TFA samples had superior uniform elongation, as well as reduction in area. Such superior tensile–ductility balance has been seen for other warm rolled steels with different compositions [15, 19, 20]. Similarly, steel wires with UFEG structures, dominated by a strong α-fiber texture, exhibit superior tensile ductility despite their high strength [21]. The steel with UFG structure created by the WCR exhibited superior reduction in area despite showing an increase in strength and a decrease in uniform elongation [15, 22]. On the other hand, the presence of finer carbide particles, homogeneously dispersed in the ferrite matrix, improves the uniform elongation characteristics of UFG steels [23, 24]. These results explain the superior ductility in the TF and TFA samples.

	Strength (GPa)		**Ductility (%)**			**Toughness (kJ/m²)**	**Strength–toughness balance (GPa × kJ/m²)**
	0.2% yield strength σ_{ys}	**Tensile strength** σ_B	**Uniform elongation** ε_u	**Total elongation** ε_t	**Reduction in area** δ	**Fracture energy** J	$\sigma_{ys} \times J$
QT	1.51	1.82	4.60	9.20	28.3	134	202
TF	1.86	1.86	7.00	14.8	40.2	5433	10105
TFA	0.99	1.06	9.80	22.0	51.3	1376	1362
SM490	0.36	0.53	18.4	30.0	79.0	2157	766

Table 1. Static mechanical properties at ambient temperature.

Figure 6 shows the *P*–*u* curves and the appearance of the samples after the bending test at ambient temperature. The cracks in the QT sample propagated directly across the center portion of the test bar, and the sample fractured with a peak loading (P_{max}) of 12.3 kN, and showed typical brittle fracture behavior. The fracture surface exhibited a quasi-cleavage of a martensite structure, as shown in **Figure 7a**. In the TF sample, the crack branched parallel to the longitudinal direction of the test bar, that is, the crack propagated vertically to the LD. The steel was not broken as shown in **Figure 6c**. The fracture surface for the crack branching planes

normal to the LD was characterized by a quasi-cleavage, and that for the planes roughly parallel to the LD was characterized by a fine dimple structure (**Figure 7b**). Namely, the fracture surface consisted of the delamination structure (⊥ LD) and the fine dimple structure (// LD). The TFA and SM490 samples exhibited fully ductile fracture as shown in **Figure 6a**. In those samples, shear lip was observed (**Figure 6d** and **e**), and the fracture surface consisted of a dimple structure. In particular, in the TFA sample, a very fine dimple structure was observed (**Figure 7c**).

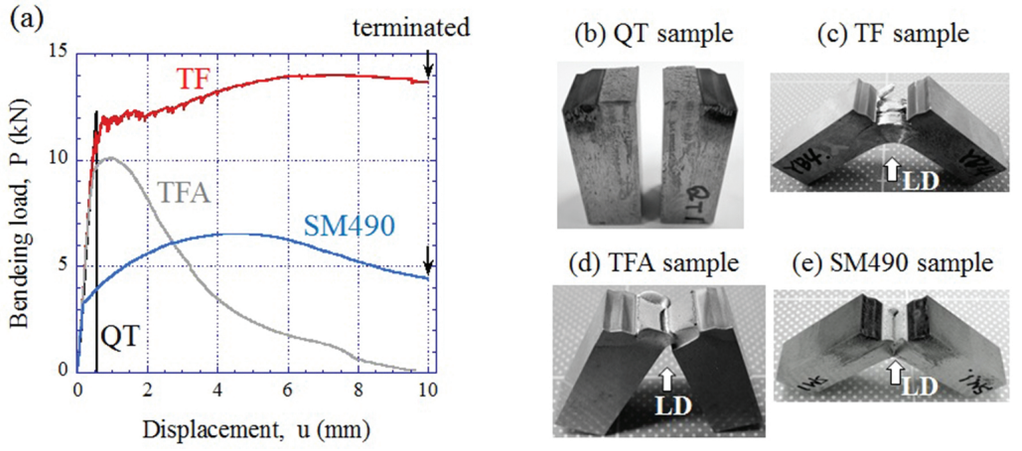

Figure 6. (a) Bending load-displacement curves at ambient temperature. (b–e) Appearance of samples after the bending test.

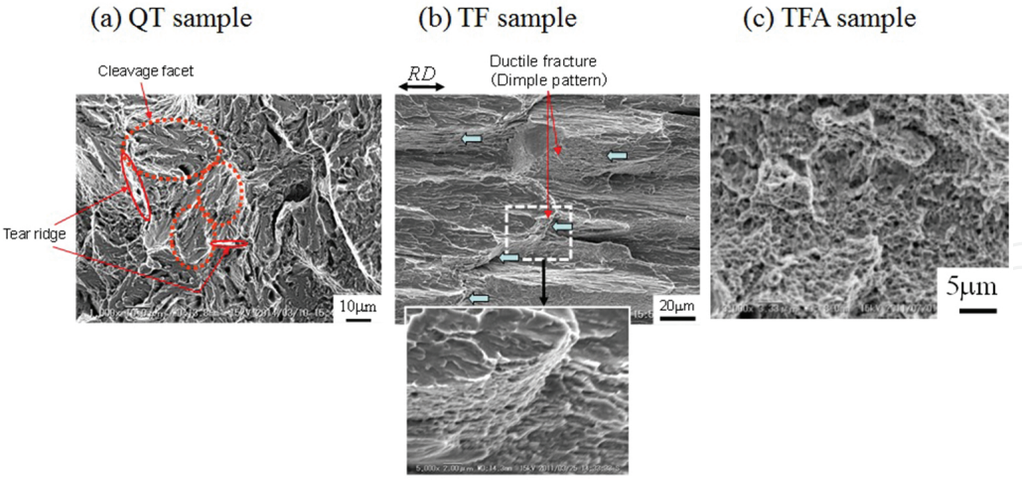

Figure 7. SEM micrographs of fracture surfaces of (a) QT, (b) TF, and (c) TFA samples.

3.2.2. Temperature dependence on strength and toughness

Figure 8 shows the yield strength, σ_{ys}, and the fracture energy, J, as a function of the test temperature for all samples. In **Figure 8a**, as is well known, the σ_{ys} increases with decreasing

http://dx.doi.org/10.5772/63797

temperature. In **Figure 8b**, it can be seen that the *J* of the QT sample is very low due to brittle fracture, regardless of temperature. The TFA and SM490 samples had a typical energy transition curve, in which the *J* decreases with decreasing temperature. Furthermore, the energy transition curve of the TFA sample is very similar to that of the SM490 sample exhibiting a DBT from −40 to −100°C, although the *J* of the TFA sample is lower than that of the SM490 sample due to a difference in strength. The result suggests that it is difficult to improve toughness by grain refinement only. On the other hand, in the TF sample, the *J* increased remarkably as the temperature decreased from 200°C, reached a maximum near ambient temperature and then decreased. Namely, the steel showed inverse temperature dependence of the toughness, such as the Charpy impact toughness reported by [2].

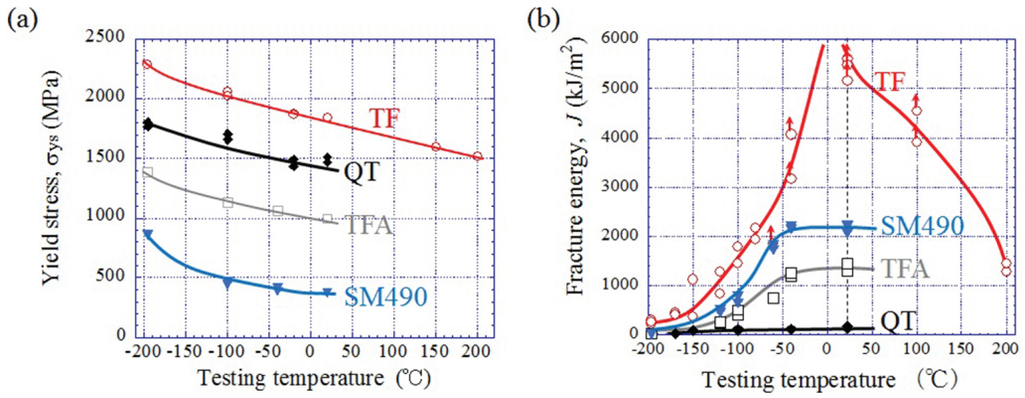

Figure 8. Variations of (a) yield strength, that is, 0.2% proof stress and (b) fracture energy with temperature. In (b), data points with upward-pointing arrows indicate that the specimens did not separate into two pieces.

4. Discussion

4.1. Crack branching and crack propagation behavior

As shown in **Table 1**, although the σ_{ys} of the TF sample improved to 1.86 GPa, compared with the QT sample, its *J* improved remarkably to 5433 kJ/m^2 and was about 40 times higher than that of the QT sample. On the contrary, the σ_{ys} of the TFA sample decreased to 0.99 GPa, and, similarly, its *J* decreased to 1376 kJ/m^2 by annealing, although it improved about 10 times more than that of the QT sample. Reduction in strength from TF to TFA samples is mainly attributed to an increase in the sizes of transverse ferrite grains and carbide particles and a decrease in dislocation density [17]. These samples had superior strength–toughness balance compared with the QT sample. In particular, the TF sample had excellent strength–toughness balance in all samples despite its highest yield strength.

Although the first load drop occurred at P_1 = 10.1 kN in the TF sample, which was smaller than the P_{max} = 12.3 kN of the QT sample, the steel exhibited a noncatastrophic fracture behavior with the evidence that the stepwise load increased beyond the P_1 and yielded a maximum load of 14 kN (**Figure 6a**). Finally, the test was terminated at u = 10 mm. In order to obtain a better

insight into the mechanism responsible for the zigzag crack propagations, an interrupted bend test was carried out. The test was stopped at u = 0.74 and 1.58 mm. **Figure 9a** presents the P–u curves in the test interrupted at u = 0.74 and 1.58 mm and also, for comparison, the curves from **Figure 6a**. Three curves for the TF sample showed the same features. The optical microscope images near the initial notch at mid-thickness for the interrupted tests at u = 0.74 and 1.58 mm and for the terminated test at u = 10 mm are shown in **Figure 9b–f**. And **Figure 9g** and **h** shows SEM images of the delaminating cracks in **Figure 9e**. It is found from **Figure 9b** that a crack started to propagate vertical to the LD, from near the initial notch root, and then the cracks propagated in a zigzag pattern along the longitudinal direction (**Figure 9c**). At u = 10 mm, many zigzag microcracks branching from the main zigzag crack, starting from the notch root were observable in the test bars (**Figure 9d**). Furthermore, some microcracks (⊥ LD and ∠45°LD) were seen ahead of and near the zigzag cracks (**Figure 9e** and **f**) [25].

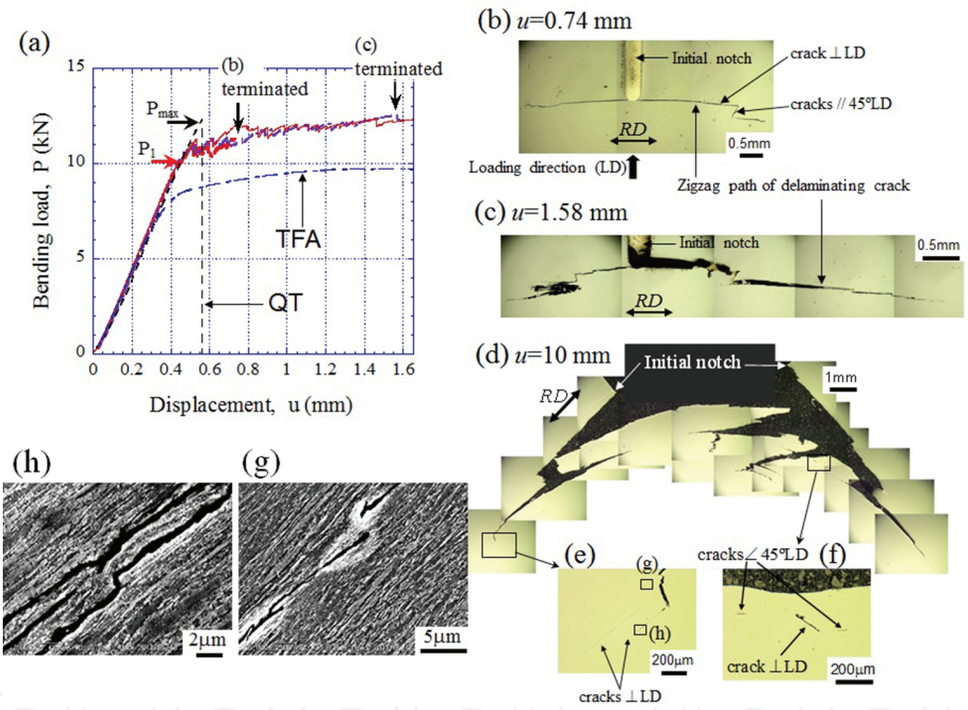

Figure 9. (a) Bending load variations in a range of u = 1.6 mm or less. OM images near the initial notch at (b) u = 0.74 mm, (c) u = 1.58 mm, and (d–f) u = 10 mm of the TF sample at mid-thickness. (g) and (h) SEM images of the delaminating crack.

In the case of laminate composites [26] having a weak interface normal to the LD (**Figure 2b**), the number of delaminations is dependent on the interfaces between layers. The ideal situation for high toughness is that all interfaces will delaminate during the applied load. As a general result, the load drops sharply after it attains the maximum value ((1)→(2) in **Figure 10**). Subsequently, a plateau region (3) in which the load becomes constant appears, and the load drops again. These load drops are due to crack propagation through the block of layers until the crack is arrested at the interfaces, and delamination along the interfaces appears as the plateau region. The extension of delamination is characterized by the ductility of the next layer,

http://dx.doi.org/10.5772/63797

where a new crack is renucleated. This pattern is repeated until the sample is fully fractured. Therefore, for delamination toughening, it is important to have not only a weak interface but also a layer with plastic deformation abilities. As seen in **Figures 6a** and **9a**, the load drops in the TF sample are very small during bending tests, and many small load drops are seen until $u = 5$ mm by increasing the load. Lath martensite, the initial microstructure in the TF sample, shows a complicated hierarchical microstructure consisting of prior austenite grains, packets, blocks, sub-blocks, and laths [17]. This characteristic is significantly different from laminate composites. The composites bonded two or more materials through fabrication have relatively straight and long interface. In the TF sample, the weak site that causes delamination is predicted to be located in an elongated {1 0 0} cleavage plane and grain boundaries [2, 15, 27]. Furthermore, a UFEG structure with RD//<1 1 0> texture has superior plastic deformation abilities. The extensive delaminating crack plane was produced with a fine dimple structure, as observed in **Figure 7b**. Namely, not only a cleavage plane (crack∠45°LD) related to {1 1 0} <1 1 0> but also a fracture plane associated with a plastic deformation was induced, together with crack ⊥ LD related to {1 0 0} <1 1 0> and grain boundaries, during the bending test. Even if many micro-cracks during the applied load occur by the presence of many cleavage planes, the propagation of micro-cracks is arrested by many grain boundaries because the UFEG structures are three-dimensionally intertwined. Under such a phenomenon, the microstructural damage is not localized, however, rather, is widely distributed over very large dimensions, such as nacre [28, 29] or bio-inspired ceramic composites [30]. In the P–u curve, many load drops, as shown in **Figure 6a**, appeared, and the P did not decrease with an increase in the u by two effects, that is, the stress shielding associated with the interference of multiple cracks and the improved plastic deformation associated with grain refinement and texture. As a result, high strength with excellent toughness was achieved in the TF sample.

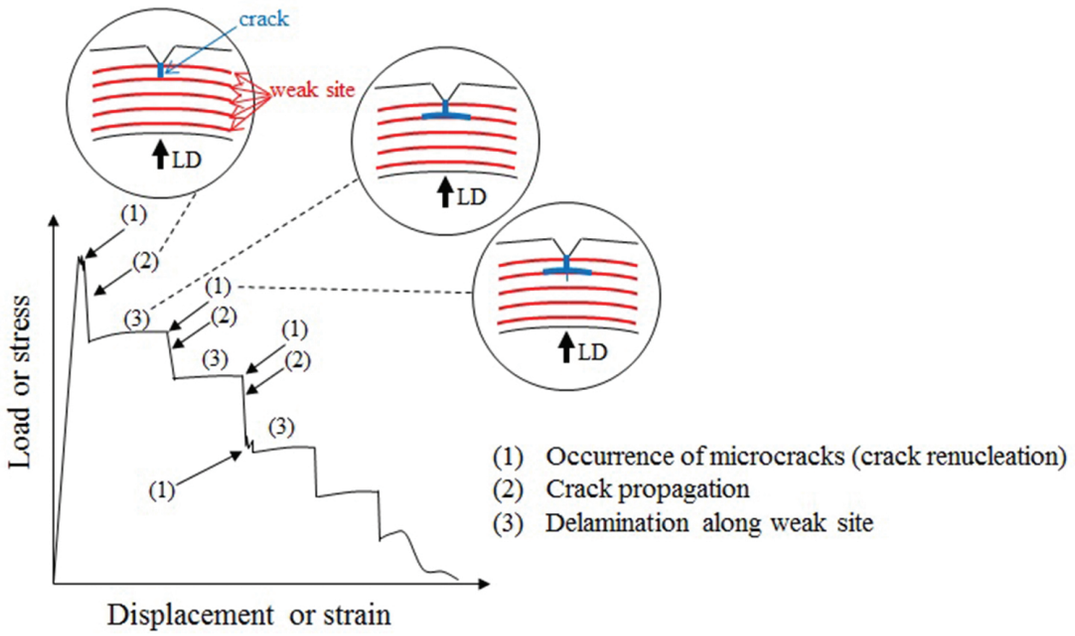

Figure 10. Typical load–displacement curve of laminate composite during three-point bend test.

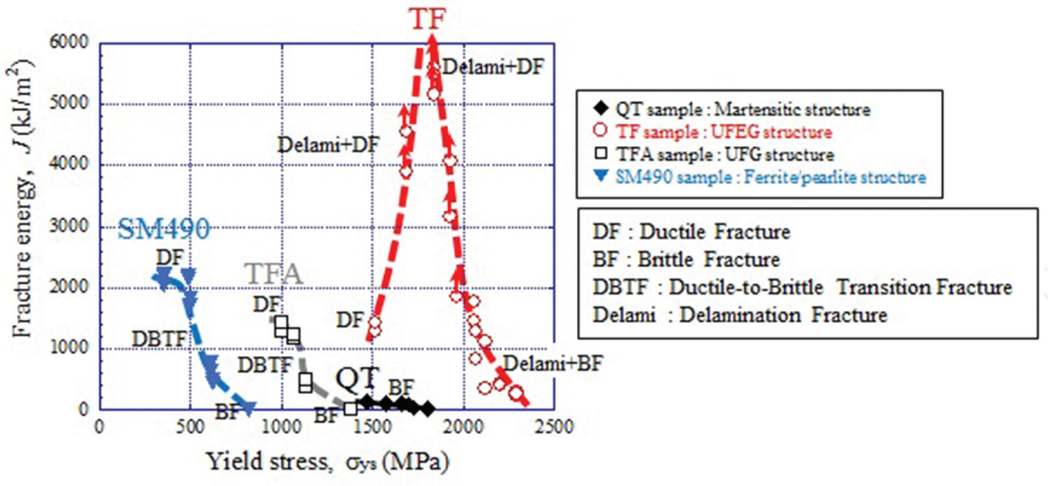

Figure 11. Strength–toughness balance for all samples. Data points with upward-pointing arrows indicate that specimens did not separate into two pieces during the bending load.

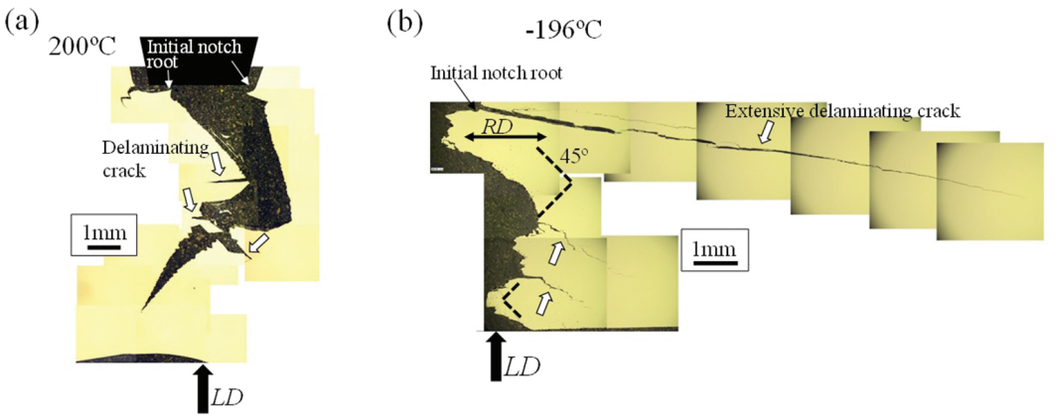

Figure 12. Cross-sectional OM images of the TF sample at mid-thickness after the bending test at (a) 200°C and (b) −196°C.

4.2. Strength–toughness balance

From the results in **Figure 8**, variations of toughness as a function of strength are obtained. **Figure 11** shows correlation between J and σ_{ys} for all samples. The results of the QT, TFA, and SM490 samples exhibited a typical strength–toughness balance. In the QT sample with strength of more than 1510 MPa, the J showed a low value of below 134 kJ/m^2 due to its brittleness at a temperature range from 23°C to −196°C. In the TF sample, first, the J increases as the σ_{ys} increases from 1500 MPa, and then it yields a maximum at near 1860 MPa which corresponds to yield strength at ambient temperature. Finally, it decreases with increasing σ_{ys}. This variation is attributed to unusual fracture behavior related to delaminating crack. The OM images of the TF sample after the bending test at 200°C and −196°C are shown in **Figure 12**. At 200°C, fracture manner exhibited ductile fracture (DF), and the crack propagated across the center portions

http://dx.doi.org/10.5772/63797

of the test bars, although some delaminating micro-cracks (arrows in **Figure 12a**) were observed. At ambient temperature (**Figure 9d**), a significant delaminating crack propagated in a zigzag pattern along the longitudinal direction (Delami + DF). This zigzag crack occurred because crack ⊥ LD and crack ∠45°LD were linked, and this behavior was repeated on the basis of the cleavage delamination mechanism. At −196°C, extensive delamination starting from the initial notch root and zigzag delaminating cracks is observable in **Figure 12b**. Macroscopically, the zigzag fracture paths appeared to have an angle of ±45° to the LD (Delami + BF). As a result, the TF sample exhibited the excellent strength–toughness balance in all samples.

In **Figure 8b**, the *J* for the TFA sample with UFG structure was lower than that for the SM490 sample with coarse grain structure, despite the same ductile fracture. **Figure 13** shows the OM images of the TFA and SM490 samples after the bending test at ambient temperature and SEM micrographs of fracture surfaces. It is found that the crack path in the TFA sample is relatively smooth compared with the crack path in the SM490 sample. As seen from SEM micrographs in **Figures 7c** and **13a**, the fracture surface in the TFA sample consists of a very fine dimple structure. On the contrary, the dimple structure of the SM490 sample observed in **Figure 13b** is larger and deeper than that of the TFA sample. Hence, low toughness of the TFA sample is attributed to difference in morphology of dimple structures related to grain size. As crystal grain becomes smaller, decrease in ductile fracture toughness is considered. The plot (DF) at σ_{ys} = 1500 MPa for the TF sample shown in **Figure 11** leads its prediction.

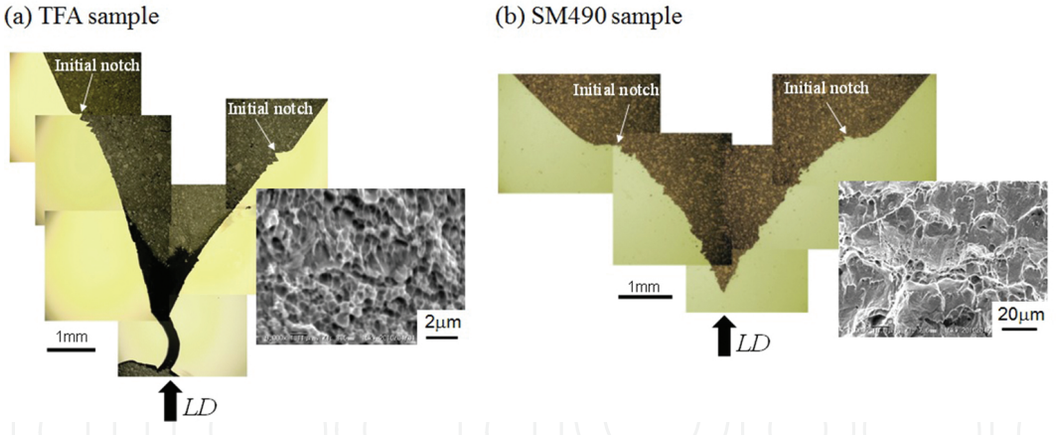

Figure 13. Cross-sectional OM images of (a) the TFA sample and (b) the SM490 sample at mid-thickness after the bending test at ambient temperature, and SEM images of fracture surfaces.

In **Figure 11**, the TF sample exhibited a ductile fracture at σ_{ys} = 1500 MPa. On the contrary, the QT sample exhibited a brittle fracture at the same strength. As a result, the *J* in the TF sample is about 10 times higher than that of the QT sample. This is attributed to a difference in the brittle fracture stresses in each direction associated with microstructural features. The brittle fracture stress, σ_F, related to weak sites such as the cleavage planes or the grain boundaries is a function of the crack size (it is replaced by the effective grain size, d_{eff}), and it is generally independent of temperature [31, 32]. Hence, the σ_F increases with the decreasing grain size. The grain size dependence of a fracture stress is higher than that of a yield stress [33]. The

brittle fracture occurs when the tensile stress near the crack tip exceeds the σ_F. Normaly, the d_{eff} of the steel with a martensitic structure such as the QT sample is reported to be packet or prior austenite grain. On the contrary, the d_{eff} of microstructures such as the TF, TFA, and SM490 samples is ferrite grain size. The tensile direction of the maximum stress near the notch induced by a bending test corresponds to the RD, as shown in **Figure 14** [34]; hence, the crack generally propagates parallel to the LD. However, in the TF sample with the UFEG structure of $d_t \ll d_L$, the $\sigma_{F//RD}$ is very higher than the $\sigma_{F//LD}$, due to $\sigma_{F//RD} \alpha d_t^{(-1/2)}$ and $\sigma_{F//LD} \alpha d_L^{(-1/2)}$. Hence, the fracture is dominated by brittle fracture stress, $\sigma_{F//LD}$, parallel to the LD. If a ductile fracture occurred before the delaminating crack, the fracture manner exhibits the DF in **Figure 11**, and the J becomes larger than that of the QT sample exhibiting the brittle fracture. On the contrary, even if the delaminating crack of σ_{LD} (the tensile stress near the notch parallel to LD) $\leq \sigma_{F//LD}$ occurred before a ductile fracture, the delamination relaxes the triaxial tensile stress near the notch and arrests the propagation crack. As a result, the J remarkably increases by the fracture manner of the Delami + DF.

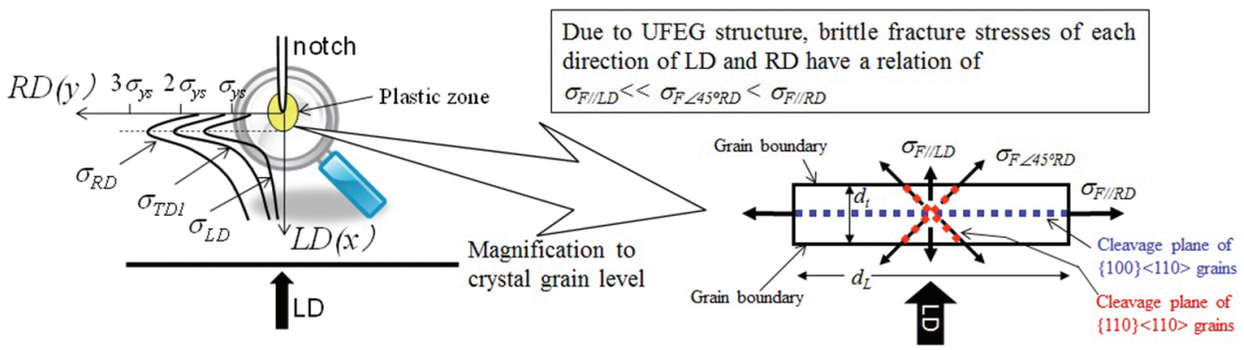

Figure 14. Schematic illustrations of (a) tensile stress triaxiality near the notch under the plane strain condition and of fracture stress for the elongated grains with a strong RD//<110>.

5. Conclusions

Low-alloy steel with an UFEG structure with an average transverse grain size of 300 nm was fabricated by multi-pass caliber rolling at 500°C, and the steel with an UFG structure with a grain size of 700 nm was fabricated by subsequent annealing at 700°C. Theses steels have yield strength, YS, of 1.86 and 0.99 GPa at ambient temperature. For comparison, two conventional steels, medium-carbon steel (YS = 1.51 GPa) with a martensitic structure and low-carbon steel (YS = 0.36 GPa) with a ferrite (20 μm)–pearlite structure, were also prepared. They were studied for the strength–toughness balance, the effect of microstructure features with respect to its balance and fracture behavior including crack propagation. The main results are as follows:

1. The fracture toughness of the UFEG steel was about 40 times higher than that of the steel with a martensitic structure, which exhibited a brittle fracture. This result is attributed to delamination toughening with many zigzag cracks. The UFG steel exhibited a fully ductile

http://dx.doi.org/10.5772/63797

fracture, and its toughness was about 10 times higher than that of the steel with a martensitic structure.

2. The strength and the toughness in the UFEG steel exhibited anisotropic properties. In particular, the toughness anisotropy was remarkable compared to the strength. The notch orientation dependence on toughness is due to differences in the spatial distribution of weak sites, such as {100} cleavage planes and boundaries of elongated grains.
3. The UFG steel and the ferrite–pearlite steel exhibited a typical energy transition curve, and the *J* of the UFG steel was lower than that of the ferrite–pearlite steel at a temperature range from 23 to −196°C. This result suggests that it is difficult to improve toughness by grain refinement only.
4. The UFEG steel showed an unusual energy curve, that is, inverse temperature dependence of the toughness, and the steel was not broken into two pieces at a temperature range from −40 to 100°C due to the fracture manner with delamination and ductile structures. The strength–toughness balance of the UFEG steel was excellent compared with that of all other steels.

Acknowledgements

We thank S. Kuroda, Y. Taniuchi, and K. Nakazato for materials processing; T. Kanno and G. Aragane for sample preparation of three-point bending test including electronic beam welding; and Ms. Yasuda for her experimental assistance in the microstructural observations. This study was supported in part by grants from the KAKENHI A (No.26249107) and the IKETANI Foundation. These grants are gratefully appreciated.

Author details

Tadanobu Inoue

Address all correspondence to: INOUE.Tadanobu@nims.go.jp

National Institute for Materials Science, Tsukuba, Japan

References

[1] Kimura Y, Inoue T, Tsuzaki K: Tempforming in medium-carbon low-alloy steel. Journal of Alloys Compounds. 2013; 577:S538–S542. DOI: 10.1016/j.jallcom.2011.12.123

[2] Kimura Y, Inoue T, Yin F, Tsuzaki, K: Inverse temperature dependence of toughness in an ultrafine grain-structure steel. Science. 2008; 320-5879: 1057–1060. DOI: 10.1126/science.1156084.

[3] Inoue T, Yanagida A, Yanagimoto J: Finite element simulation of accumulative roll-bonding process. Materials Letters. 2013; 106: 37–40. DOI: 10.1016/j.matlet.2013.04.093

[4] Inoue T, Horita Z, Somekawa H, Ogawa K: Effect of initial grain sizes on hardness variation and strain distribution of pure aluminum severely deformed by compression tests. Acta Materialia. 2008; 56(20): 6291–6303. DOI: 10.1016/j.actamat.2008.08.042

[5] Takaki S, Kawasaki K, Kimura Y: Mechanical properties of ultra fine grained steels. Journal of Materials Processing Technology. 2001; 117(3): 359–363. DOI: 10.1016/S0924-0136(01)00797-X

[6] Nagai K: Ultrafine-grained ferrite steel with dispersed cementite particles. Journal of Materials Processing Technology. 2001; 117(3): 329–332. DOI: 10.1016/S0924-0136(01)00789-0

[7] Song R, Ponge D, Raabe D: Mechanical properties of an ultrafine grained C–Mn steel processed by warm deformation and annealing. Acta Materialia. 2005; 53(18): 4881–4892. DOI: 10.1016/j.actamat.2005.07.009

[8] Tsuji N, Okuno S, Koizumi Y, Minamino Y: Toughness of ultrafine grained ferritic steels fabricated by ARB and annealing process. Material Transactions. 2004; 45(7): 2272–2281.

[9] Fujioka M, Abe Y, Hagiwara Y: Refinning of ferrite grain by using of transformation or recrystallization induced by heavy deformation. CAMP–ISIJ. 2000; 13: 1136–1139.

[10] Heiser F A, Hertzberg R W: Structural control and fracture anisotropy of banded steel. Journal of Iron Steel Institute. 1971; 209: 975–980

[11] McNicol R C: Correlation of Charpy test results for standard and nonstandard size specimens. Welding Journal. 1965; 44: 385–393.

[12] Bourell D L: Cleavage delamination in impact tested warm-rolled steel. Metallurgical and Materials Transactions A. 1983; 14: 2487–2496. DOI: 10.1007/BF02668890

[13] Rao K T V, Ritchie R O: Mechanical properties of Al–Li alloys. Part 1. Fracture toughness and microstructure. Materials Science and Technology. 1989; 5(9): 882–895. DOI: 10.1179/mst.1989.5.9.882

[14] Launey M E, Ritchie R O: On the fracture toughness of advanced materials. Advanced Materials. 2009; 21(20): 2103–2110. DOI: 10.1002/adma.200803322

[15] Inoue T, Yin F, Kimura Y, Tsuzaki K, Ochiai S: Delamination effect on impact properties of ultrafine-grained low carbon steel processed by warm caliber rolling. Metallurgical and Materials Transactions A. 2010; 41: 341–355. DOI: 10.1007/s11661-009-0093-x

[16] Inoue T, Yin F, Kimura Y: Strain distribution and microstructural evolution in multi-pass warm caliber rolling. Materials Science and Engineering A. 2007; 466: 114–122. DOI: 10.1016/j.msea.2007.02.098

[17] Kimura Y, Inoue T, Yin F, Tsuzaki K. Supporting online material for [2]. www.sciencemag.org/cgi/content/full/320/5879/1057/DC1

[18] Inoue T, Kimura Y: Toughening of low-carbon steel by ultrafine-grained structure. Transactions of the Japan Society of Mechanical Engineers, Series A. 2013; 79(804): 1226–1238 (in Japanese).

[19] Tsuchida N, Inoue T, Enami K: Estimations of the true stress and true strain until just before fracture by the stepwise tensile test and Bridgman equation for various metals and alloys. Materials Transactions. 2012; 53: 133–139. DOI: 10.2320/matertrans.MD201112

[20] Lee T, Park C H, Lee D L, Lee C S: Enhancing tensile properties of ultrafine-grained medium-carbon steel utilizing fine carbides. Materials Science and Engineering A. 2011; 528: 6558. DOI: 10.1016/j.msea.2011.05.007

[21] Yutori T, Katsumata M, Kanetsuki Y: Bull. JIM. 1989; 28: 313 (in Japanese)

[22] Torizuka S, Muramatsu E, Murty S V S N, Nagai K: Microstructure evolution and strength-reduction in area balance of ultrafine-grained steels processed by warm caliber rolling. Scripta Materialia. 2006; 55: 751–754. DOI: 10.1016/j.scriptamat.2006.03.067

[23] Oh Y S, Son I H, Jung K H, Kim D K, Lee D L, Im Y T: Effect of initial microstructure on mechanical properties in warm caliber rolling of high carbon steel. Materials Science and Engineering A. 2011; 528: 5833–5839. DOI: 10.1016/j.msea.2011.04.016

[24] Ohmori A, Torizuka S, Nagai K: Strain-hardening due to dispersed cementite for low carbon ultrafine-grained steels. ISIJ International. 2004; 44(6): 1063–1071. DOI: 10.2355/isijinternational.44.1063

[25] Inoue T, Kimura Y, Ochiai S: Shape effect of ultrafine-grained structure on static fracture toughness in low-alloy steel. Science and Technology of Advanced Materials. 2012; 13(3): 035005. DOI: 10.1088/1468-6996/13/3/035005

[26] Pozuelo M, Carreno F, Ruano O A: Delamination effect on the impact toughness of an ultrahigh carbon–mild steel laminate composite. Composite Science and Technology. 2006; 66: 2671. DOI: 10.1016/j.compscitech.2006.03.018

[27] Kimura Y, Inoue T, Yin F, Tsuzaki K: Delamination toughening of ultrafine grain structure steels processed through tempforming at elevated temperatures. ISIJ International. 2010; 50: 152–161. DOI: 10.2355/isijinternational.50.152

[28] Meyers M A, Chen P Y, Lin A Y, Seki Y: Biological materials: structure and mechanical properties. Progress Materials Science. 2008; 53: 1–260. DOI: 10.1016/j.pmatsci.2007.05.002

[29] Kakisawa H, Sumitomo T: The toughening mechanism of nacre and structural materials inspired by nacre. Science and Technology of Advanced Materials. 2011; 12: 064710. DOI: 10.1088/1468-6996/12/6/064710

[30] Munch E, Launey M E, Alsem D H, Saiz E, Tomsia A P, Ritchie R O: Tough, bio-inspired hybrid materials. Science. 2008; 322: 1516–1520. DOI: 10.1126/science.1164865

[31] Ma H: The effect of stress triaxiality on the local cleavage fracture stress in a granular bainitic weld metal. International Journal of Fracture. 1998; 89:143. DOI: 10.1023/A:1007484026645

[32] Kameda J, Nishiyama Y: Combined effects of phosphorus segregation and partial intergranular fracture on the ductile–brittle transition temperature in structural alloy steels. Materials Science and Engineering A. 2011; 528: 3705–3713. DOI: 10.1016/j.msea.2011.01.018

[33] Gillbert A, Hahn G T, Reid C N, Wizcox R A: Twin-induced grain boundary cracking in b.c.c. metals. Acta Metallurgica. 1964; 12(6): 754–755. DOI: 10.1016/0001-6160(64)90230-5

[34] Inoue T, Kimura Y: Effect of initial notch orientation on fracture toughness in fail-safe steel. Journal of Materials Science. 2013; 48(13): 4766–4772. DOI: 10.1007/s10853-012-6874-4